Check for updates

Advanced Functional Materials

ADVANCED FUNCTIONAL MATERIALS
www.afm-journal.de

RESEARCH ARTICLE

Ni-Regulated Partial Reconstruction of Hydrated Vanadium Oxide for Fast and Durable Aqueous Zinc-Ion Batteries

Zhihan Kong[1,2] | Penghua Liang[3] | Tengyu Yao[2] | Xinyue Mu[1] | Dingwei Ji[1,2] | Longbiao Yu[1,2] | Feier Wang[1] | Jing Wang[1] | Kang Yan[1] | Jun Guo[1] | Laifa Shen[2] | Linfeng Hu[4] | Kongjun Zhu[1]

[1]State Key Laboratory of Mechanics and Control for Aerospace Structures, College of Aerospace Engineering, Nanjing University of Aeronautics and Astronautics, Nanjing, China | [2]College of Materials Science and Technology, Nanjing University of Aeronautics and Astronautics, Nanjing, China | [3]Huzhou Key Laboratory of Green Energy Materials and Battery Cascade Utilization, School of Intelligent Manufacturing, Huzhou College, Huzhou, China | [4]School of Materials Science and Engineering, Southeast University, Nanjing, China

Correspondence: Jun Guo (junguo@nuaa.edu.cn) | Laifa Shen (lfshen@nuaa.edu.cn) | Linfeng Hu (linfenghu@seu.edu.cn) | Kongjun Zhu (kjzhu@nuaa.edu.cn)

Received: 14 August 2026 | **Revised:** 2 September 2026 | **Accepted:** 21 September 2026

Keywords: aqueous zinc-ion batteries | high-temperature mixing hydrothermal | hydrated vanadium oxides | interlayer regulation | ion incorporation

ABSTRACT

Reconciling rapid Zn^{2+} transport with structural durability remains challenging for layered vanadium-oxide cathodes. In this work, a one-step high-temperature mixing hydrothermal strategy couples the glucose-induced reductive reconstruction of V_2O_5 with synchronous Ni^{2+} incorporation, producing a Ni-regulated $H_2V_3O_8$-derived hydrated vanadium oxide (NiVOH) within 1 h at 240°C. Density functional theory screening of five guest cations identifies Ni^{2+} as providing the lowest Zn^{2+} migration barrier and enhanced electronic states near the Fermi level, consistent with comparative electrochemical measurements. Structural analyses reveal coexisting $H_2V_3O_8$ and Ni-containing hydrated domains, accompanied by increased structural water and oxygen-vacancy-related defects. This domain-balanced architecture preserves accessible hydrated galleries while restraining cycling-induced deformation. NiVOH consequently delivers 433.4 mAh g^{-1} after 50 cycles at 0.1 A g^{-1} and sustains 282.6 mAh g^{-1} after 6000 cycles at 10 A g^{-1}. In situ x-ray diffraction and real-time fiber-optic strain monitoring further reveal reversible lattice breathing and substantially reduced electrode-level strain fluctuations. This work establishes rapid coupled reconstruction and guest-ion regulation as an effective route for balancing ion accessibility and mechanical stability in layered aqueous battery cathodes.

1 | Introduction

The rapid growth of renewable energy technologies has created an urgent demand for safe, low-cost, and environmentally benign electrochemical energy storage systems. Although lithium-ion batteries have achieved great success in portable electronics and electric vehicles, flammable organic electrolytes and limited lithium resources restrict their further deployment in large-scale energy storage [1–4]. In this regard, aqueous zinc-ion batteries (AZIBs) have attracted increasing attention because of the intrinsic safety of aqueous electrolytes and the low cost and high theoretical capacity of Zn metal anodes [5–7]. However, the practical application of AZIBs is still limited by the lack of cathode materials that can simultaneously deliver high capacity and long-term cycling stability [6–9].

Layered vanadium oxides are among the most promising cathode candidates for AZIBs, owing to the multiple redox states of vanadium and their open frameworks for ion insertion/extraction [8–12]. In particular, V_2O_5 represents a typical layered vanadium oxide with high theoretical capacity and abundant redox-active sites [13–15]. However, pristine V_2O_5 usually suffers from narrow

All rights reserved, including rights for text and data mining and training of artificial intelligence technologies or similar technologies.
© 2026 Wiley-VCH GmbH

interlayer spacing, strong electrostatic interactions between Zn^{2+} and the V–O host framework, and large structural distortion during repeated charge/discharge processes [11–18]. Under these circumstances, intercalating guest species into the interlayer space of V_2O_5 has been widely adopted as an effective strategy to improve its zinc-storage performance [13–25]. Chen et al. prepared $Ru_{0.2}V_2O_5{\cdot}0.41H_2O$, in which Ru^{3+} pre-intercalation strengthened the hydrated layers and regulated carrier migration, thereby suppressing vanadium dissolution and retaining 98.2% of the capacity over 5000 cycles at 10 A g^{-1} [26]. However, the preparation of interlayer-engineered V_2O_5-based cathodes commonly relies on H_2O_2-assisted dissolution of V_2O_5, which usually involves complicated solution chemistry and long reaction periods [18–26].

Compared with pristine V_2O_5, hydrated $H_2V_3O_8$ possesses a more open layered framework and intrinsic structural water, which can provide expanded ion-transport channels and partially screen the strong interaction between Zn^{2+} and the host lattice [27–32]. Zhang et al. introduced Sn^{4+} into $V_3O_7{\cdot}H_2O$, where Sn-containing pillars increased the calculated VO^{2+} dissolution energy and improved electronic and Zn^{2+}-transport kinetics; the cathode delivered 408 mAh g^{-1} at 0.1 A g^{-1} and retained 89.3% capacity over 6000 cycles at 5 A g^{-1} [33]. Despite these advances, current strategies for constructing guest-ion-regulated hydrated vanadium oxides generally rely on multistep dissolution–reassembly processes, prolonged hydrothermal reactions, or additional heat treatments [33–38]. These synthetic constraints not only reduce processing efficiency but also make it difficult to synchronize phase reconstruction with guest-ion incorporation, thereby limiting precise control over the hydrated framework and interlayer chemistry. Therefore, developing a rapid and controllable route that can convert V_2O_5 into a hydrated layered framework while simultaneously introducing stabilizing guest ions is essential for reconciling fast Zn^{2+} transport with long-term structural durability [27, 28].

Herein, we report a dual-chamber-assisted rapid high-temperature mixing hydrothermal strategy to synthesize Ni^{2+}-intercalated $H_2V_3O_8$-derived hydrated vanadium oxide (NiVOH). Unlike conventional hydrothermal methods, our approach spatially separates V_2O_5 from the glucose/Ni^{2+} precursor solution at the initial stage and enables rapid mixing under high-temperature hydrothermal conditions. During this process, glucose promotes the reductive reconstruction of V_2O_5 into a hydrated vanadium oxide with a more open layered framework, while Ni^{2+} is simultaneously incorporated into the interlayer region as structural pillars. The resulting NiVOH exhibits an optimized layered structure, enriched oxygen vacancies, and enhanced Zn^{2+} diffusion kinetics. Benefiting from the Ni^{2+}-regulated framework and rapid reconstruction process, NiVOH delivers high reversible capacity, excellent rate capability, and long-term cycling stability in AZIBs. Furthermore, in situ XRD and fiber-optic strain monitoring reveal that Ni^{2+} intercalation effectively mitigates structural evolution and strain fluctuation during cycling, leading to more stable Zn^{2+} storage behavior. This work provides a rapid and efficient strategy for constructing ion-intercalated layered vanadium oxide cathodes for high-performance aqueous zinc-ion batteries.

2 | Results and Discussion

2.1 | DFT Calculations and Synthesis of Materials

Previous studies have identified Ni^{2+} as a promising interlayer guest for hydrated vanadium oxides because its strong oxygen coordination stabilizes Ni–O linkages, while its partially occupied $3d^8$ states facilitate electronic-structure modulation of the host [13, 14, 39–41]. To better clarify the role of interlayer cations and rationalize the selection of Ni^{2+}, density functional theory (DFT) calculations were performed on pristine $H_2V_3O_8$ and several metal-ion-intercalated models. Since lattice oxygen directly interacts with inserted Zn^{2+}, the O p-band center was first analyzed. As shown in Figure 1a, NiVOH exhibits the highest O p-band center among the investigated samples, indicating that Ni^{2+} intercalation effectively modulates the electronic structure of lattice oxygen and optimizes the interaction between Zn^{2+} and O within the layered framework [42, 43]. Meanwhile, the V d-band center of NiVOH is also higher than that of pristine $H_2V_3O_8$ and other intercalated models (Figure 1b), suggesting improved electronic regulation of the redox-active V sites. This distinct electronic modulation can be associated with the partially occupied $3d^8$ configuration of Ni^{2+}, which provides accessible d states for orbital interaction with neighboring O 2p states. The resulting Ni–O interaction promotes local charge redistribution through the Ni–O–V linkage, thereby coupling the electronic states of O and V and producing more pronounced shifts of the O p-band and V d-band centers [42–44]. The Zn^{2+} diffusion behavior was further evaluated by calculating the migration energy barriers. As shown in Figure 1c, NiVOH presents the lowest diffusion barrier, demonstrating that Ni^{2+} intercalation provides a more favorable pathway for Zn^{2+} migration and thus accelerates ion diffusion kinetics. The density of states (DOS) further confirms the electronic advantage of NiVOH. Pristine $H_2V_3O_8$ shows a band gap of 0.38 eV near the Fermi level (Figure 1d), whereas NiVOH displays enhanced electronic states around the Fermi level with an almost vanished band gap (Figure 1e), indicating improved electronic conductivity after Ni^{2+} incorporation [16–18]. Furthermore, the charge density difference of NiVOH reveals obvious electron accumulation and depletion around the inserted Ni species and adjacent V–O layers (Figure 1f and Figure S1), evidencing strong electronic coupling and enhanced charge transfer between Ni^{2+} and the host framework [39, 40]. These theoretical results collectively indicate that Ni^{2+} intercalation can simultaneously optimize the oxygen and vanadium electronic structures, lower the Zn^{2+} diffusion barrier, and improve charge transport.

Therefore, Ni^{2+} was selected as the preferred guest cation for constructing high-performance hydrated vanadium oxide. As illustrated in Figure 2, NiVOH and the corresponding control samples were synthesized through a dual-chamber-assisted one-step high-temperature mixing hydrothermal process. Specifically, this strategy spatially separates V_2O_5 from the glucose/Ni^{2+} precursor solution in two independent compartments of the autoclave liner. During the heating stage, V_2O_5 and the glucose/Ni^{2+} precursor are spatially separated, which helps minimize premature reactions and precipitation before the target temperature is reached. After the system reaches 240°C, the two precursor components are rapidly mixed under hydrothermal conditions. At

16163028, 0, Downloaded from https://advanced.onlinelibrary.wiley.com/doi/10.1002/adfm.78757 by Southeast University, Wiley Online Library on [10/10/2026]. See the Terms and Conditions (https://onlinelibrary.wiley.com/terms-and-conditions) on Wiley Online Library for rules of use; OA articles are governed by the applicable Creative Commons License

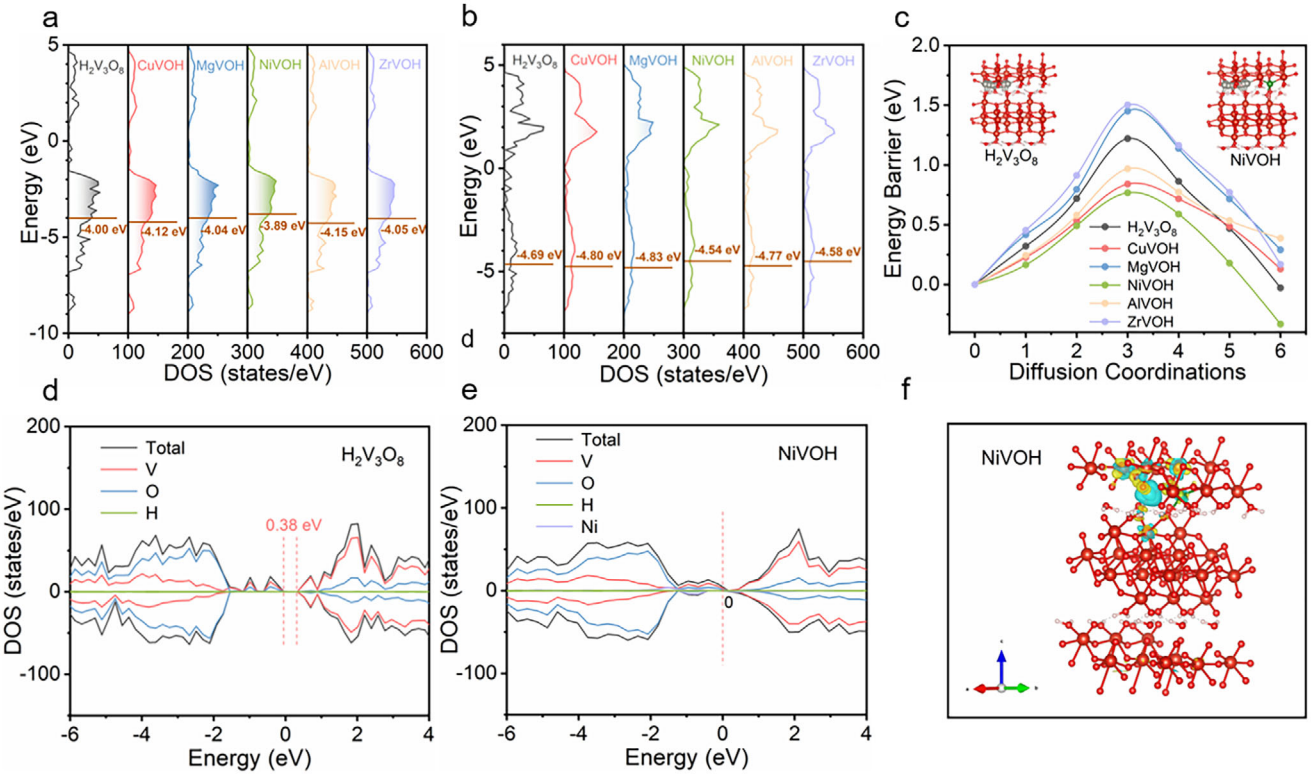

FIGURE 1 | DFT calculations: (a) The p-band center values of O, (b) d-band center values of V, (c) Zn^{2+} diffusion barriers along the migration pathway in pristine $H_2V_3O_8$, CuVOH, MgVOH, NiVOH, AlVOH, and ZrVOH. Total and projected density of states of (d) pristine $H_2V_3O_8$ and (e) NiVOH. (f) Charge density difference of NiVOH. Yellow and blue areas correspond to the loss and gain of charge, respectively.

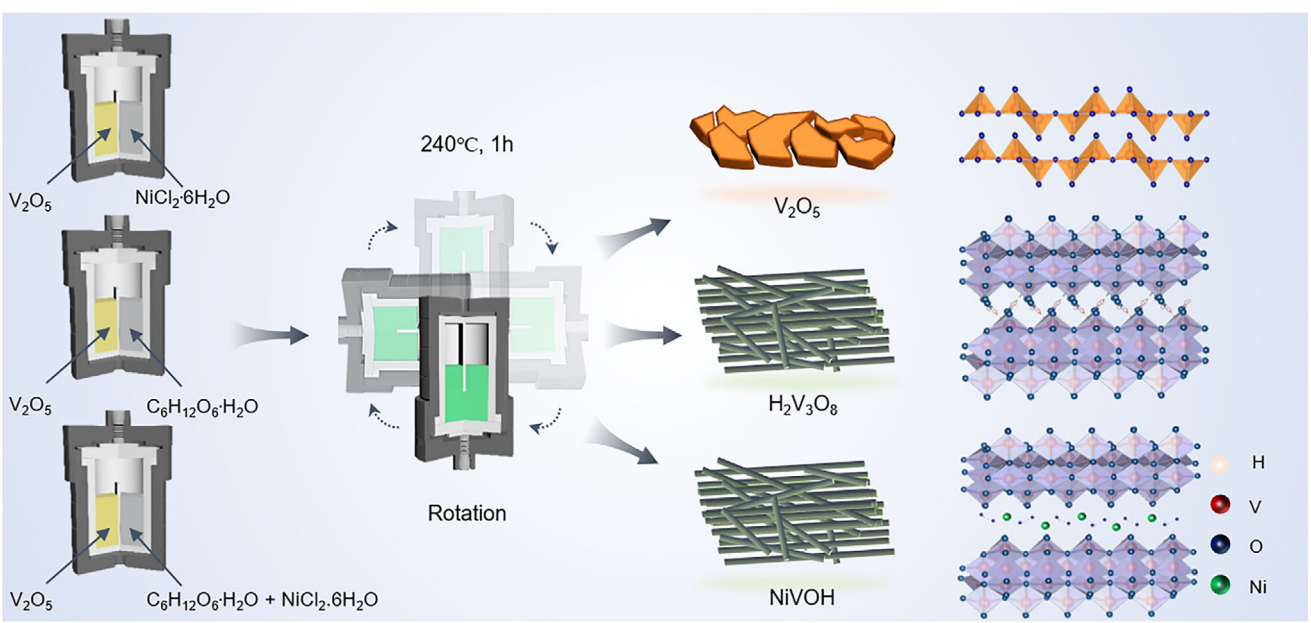

FIGURE 2 | Schematic illustration of the synthesis of different samples.

this stage, glucose-induced reconstruction of the V–O framework and Ni^{2+} incorporation can proceed simultaneously [30, 34]. As a result, Ni^{2+}-intercalated hydrated vanadium oxide, denoted as NiVOH, can be obtained after hydrothermal treatment at 240°C for only 1 h. Control experiments further verify the indispensable roles of glucose and $NiCl_2{\cdot}6H_2O$ in this process. When Ni^{2+} was introduced in the absence of glucose, the product remained as pure V_2O_5, indicating that the rigid V_2O_5 framework is difficult to reconstruct or effectively intercalate under such a short hydrothermal reaction. In contrast, the sample prepared with

16163028, 0, Downloaded from https://advanced.onlinelibrary.wiley.com/doi/10.1002/adfm.78757 by Southeast University, Wiley Online Library on [10/10/2026]. See the Terms and Conditions (https://onlinelibrary.wiley.com/terms-and-conditions) on Wiley Online Library for rules of use; OA articles are governed by the applicable Creative Commons License

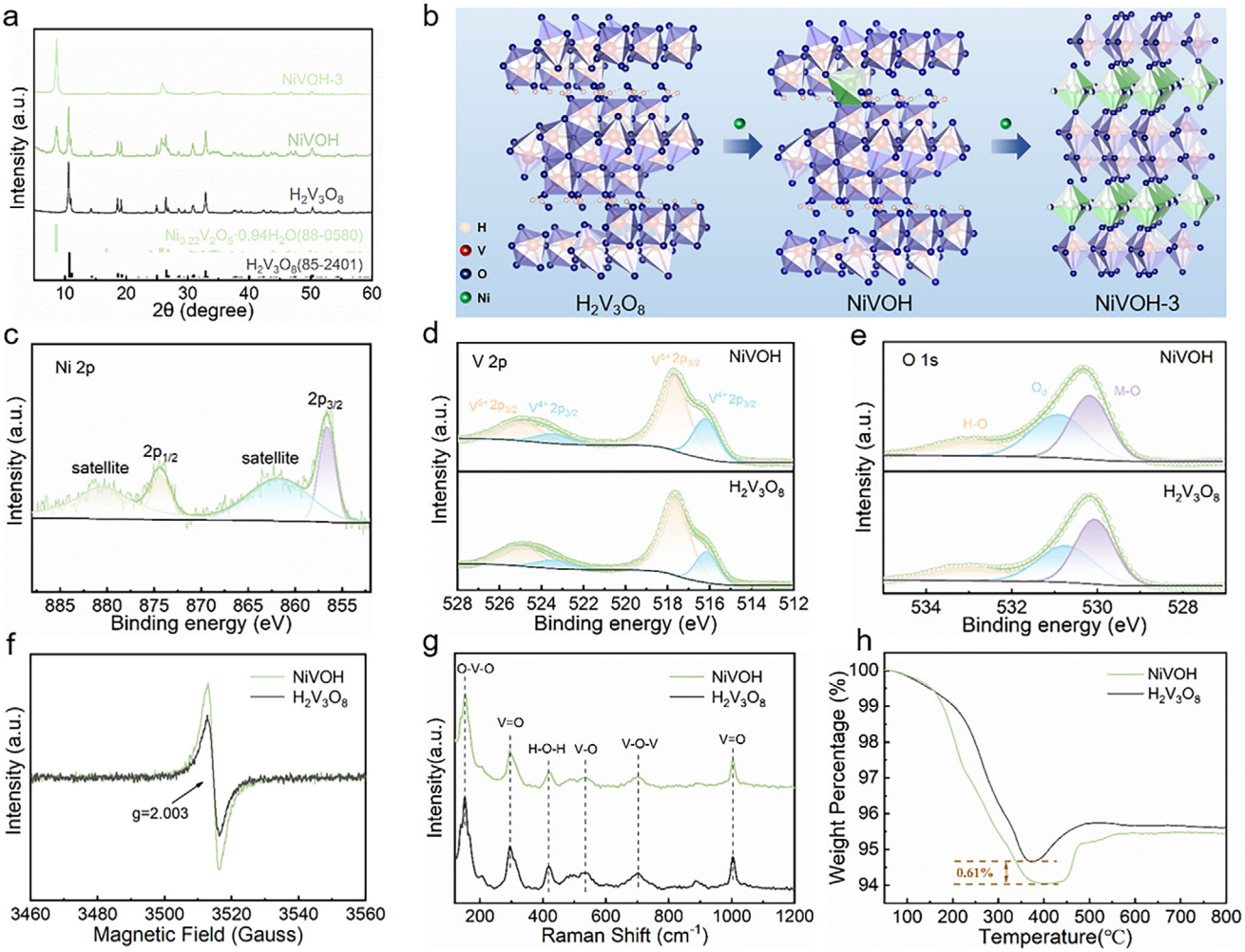

FIGURE 3 | Structural and chemical characterization: (a) XRD patterns of $H_2V_3O_8$, NiVOH (Ni:V = 0.05:1), and NiVOH-3 (Ni:V = 0.1:1). (b) Schematic illustration of the structural evolution with increasing Ni incorporation. (c) High-resolution Ni 2p XPS spectrum of NiVOH. High-resolution XPS spectra of (d) V 2p and (e) O 1s for $H_2V_3O_8$ and NiVOH. (f) EPR spectra and (g) Raman spectra of $H_2V_3O_8$ and NiVOH. (h) TGA curves of $H_2V_3O_8$ and NiVOH measured in air.

glucose but without $NiCl_2{\cdot}6H_2O$ was converted into pure $H_2V_3O_8$, confirming the ability of glucose to drive the transformation of V_2O_5 into a hydrated layered vanadium oxide. These results demonstrate that the formation of NiVOH relies on the synergistic coupling between glucose-induced structural reconstruction and synchronous Ni^{2+} interlayer incorporation.

2.2 | Characterization of Materials

X-ray diffraction (XRD) was employed to examine the structural evolution induced by Ni incorporation. As shown in Figure 3a, the pristine sample exhibits the characteristic diffraction pattern of $H_2V_3O_8$. After Ni incorporation, the major reflections of NiVOH remain consistent with those of $H_2V_3O_8$, indicating that the host framework is largely retained. Meanwhile, several additional weak reflections emerge, suggesting limited local reconstruction associated with Ni incorporation. When the Ni content is further increased, these new reflections become more pronounced, and NiVOH-3 gradually evolves toward a nickel-vanadate-like hydrated structure. Inductively coupled plasma optical emission spectroscopy (ICP-OES) analysis further gives Ni/V molar ratios of approximately 0.045 and 0.092 for NiVOH and NiVOH-3, respectively (Table S1). Therefore, their nominal compositions are assigned as $Ni_{0.13}V_3O_7$ and $Ni_{0.18}V_2O_5$, respectively. The corresponding structural evolution is schematically illustrated in Figure 3b. Rather than simply expanding the parent lattice, Ni incorporation progressively reorganizes the V–O polyhedra [14, 39, 40]. The partially reconstructed NiVOH framework is expected to preserve accessible ion-transport galleries while providing additional structural anchoring, thereby balancing ion accessibility and framework stability.

The successful incorporation of Ni is corroborated by the Ni signal in the x-ray photoelectron spectroscopy (XPS) survey spectrum (Figure S2) and the high-resolution Ni 2p spectrum (Figure 3c). Besides, V 2p analysis reveals a pronounced increase in the V^{4+} fraction after Ni incorporation (Figure 3d), indicating partial reduction of vanadium and substantial charge redistribution within the host framework. Meanwhile, the defect-related component in the O 1s spectrum becomes more prominent for NiVOH (Figure 3e). This observation is supported by the intensified

16163028, 0, Downloaded from https://advanced.onlinelibrary.wiley.com/doi/10.1002/adfm.78757 by Southeast University, Wiley Online Library on [10/10/2026]. See the Terms and Conditions (https://onlinelibrary.wiley.com/terms-and-conditions) on Wiley Online Library for rules of use; OA articles are governed by the applicable Creative Commons License

electron paramagnetic resonance (EPR) response at $g = 2.003$, which is associated with oxygen-vacancy-related paramagnetic centers (Figure 3f) [45, 46]. The coupled increase in V^{4+} and oxygen vacancies demonstrates that Ni incorporation induces not only structural reconstruction but also pronounced electronic and defect regulation, which can provide additional charge carriers and electrochemically accessible sites [45–47].

Raman spectra in Figure 3g show that both samples retain the characteristic vibrations of the vanadium–oxygen framework, whereas the V—O-related bonds of NiVOH exhibit noticeably reduced intensities, further indicating that Ni incorporation perturbs the local coordination environment and induces structural reconstruction. Consistently, the Fourier transform infrared spectroscopy (FTIR) spectra in Figure S3 display weakened V═O and V—O—V vibration peaks after Ni incorporation, together with enhanced H_2O-related peaks, suggesting an increased degree of hydration [33–35]. Thermogravimetric analysis (TGA) conducted in air further supports this conclusion. NiVOH exhibits a larger mass loss in the water-release region than $H_2V_3O_8$, and this trend becomes more pronounced for NiVOH-3 (Figure 3h and Figure S4), indicating increased water-related content and a higher overall degree of hydration with progressive Ni incorporation. During subsequent heating in air, the Ni-containing samples display a more evident mass recovery, which is attributed to oxygen uptake during the reoxidation of reduced vanadium species [26, 33]. This behavior is consistent with the increased V^{4+} fraction revealed by XPS. Collectively, these results demonstrate that Ni incorporation drives a progressive structural and electronic reconstruction, yielding a hydrated, defect-rich, and Ni-anchored vanadium oxide framework.

Scanning electron microscopy (SEM) images reveal that NiVOH consists of densely interwoven nanorods with relatively uniform dimensions (Figure 4a). Comparison with the pristine $H_2V_3O_8$ and NiVOH samples at different magnifications shows no substantial change in the overall morphology after Ni incorporation (Figure S5). The rod-like architecture of NiVOH is further confirmed by the transmission electron microscopy (TEM) image (Figure 4b). Two distinct sets of lattice fringes are resolved in the HRTEM images. The interplanar spacings of 0.344 and 0.826 nm can be assigned to the (003) plane of the nickel-vanadate-like hydrated phase and the (110) plane of $H_2V_3O_8$, respectively (Figure 4c,d). Their coexistence within the same nanorod provides direct evidence that NiVOH contains both reconstructed Ni-containing domains and residual $H_2V_3O_8$ structural motifs, consistent with the XRD results. The scanning transmission electron microscopy (STEM) image and corresponding elemental mappings show homogeneous distributions of V, O, and Ni throughout the nanorod without evident Ni-rich aggregation (Figure 4e–h and Figure S6), further confirming the uniform incorporation of Ni. The concentric diffraction rings in the selected-area electron diffraction (SAED) pattern can be indexed to the (210), (211), and (711) planes of $H_2V_3O_8$ (Figure 4i). The N_2 adsorption–desorption measurements further reveal an increased Brunauer–Emmett–Teller (BET) surface area from 28.31 $m^2\ g^{-1}$ for $H_2V_3O_8$ to 36.65 $m^2\ g^{-1}$ for NiVOH (Figure 4j,k). The more pronounced mesoporous contribution of NiVOH may enhance electrolyte penetration and facilitate ion transport by improving the accessibility of electrochemically active interfaces [47, 48].

2.3 | Characterization of Electrochemical Performance

The Zn-storage behavior of NiVOH was first evaluated by cyclic voltammetry (CV). As shown in Figure 5a, two pairs of redox peaks are observed at approximately 0.61/0.69 and 0.85/1.04 V, reflecting multistep ion insertion/extraction coupled with reversible changes in the vanadium oxidation state [26, 32, 36]. An additional anodic peak appears near 1.55 V during the first scan but almost disappears in the subsequent cycles, suggesting an irreversible initial electrochemical activation-related process [27, 33]. The close overlap of the second to fourth CV curves indicates that highly reversible electrochemical reactions are established after the initial activation process.

The cycling performance at 0.1 A g^{-1} further demonstrates the capacity enhancement achieved by Ni incorporation (Figure 5b). After 50 cycles, NiVOH maintains a reversible specific capacity of 433.4 mAh g^{-1}, substantially higher than the 332.5 mAh g^{-1} delivered by $H_2V_3O_8$. The galvanostatic charge–discharge (GCD) profiles of NiVOH recorded at different cycles exhibit similar shapes and a high degree of overlap (Figure 5c), consistent with the multistep redox behavior observed in the CV curves. The performance advantage of NiVOH becomes more pronounced under high-rate operation. As displayed in Figure 5d, NiVOH undergoes a brief activation process and subsequently exhibits stable cycling with a Coulombic efficiency (CE) approaching 100% at 10 A g^{-1}. This activation may arise from progressively improved electrolyte penetration and the gradual utilization of initially less-accessible redox sites during cycling, while stronger initial polarization and incomplete active-material utilization make the capacity increase more pronounced at high current densities [46–48]. Even after 6000 cycles, NiVOH retains a high specific capacity of 282.6 mAh g^{-1}, whereas $H_2V_3O_8$ delivers only 205.1 mAh g^{-1}. Such outstanding high-rate durability indicates that the Ni-regulated interlayer configuration and the resulting partially reconstructed framework can accommodate rapid and repeated ion insertion/extraction while mitigating progressive structural degradation during prolonged cycling [30–35, 49]. NiVOH also exhibits markedly improved rate capability (Figure 5e). At current densities of 0.1, 0.2, 0.5, 1, 2, 5, and 10 A g^{-1}, NiVOH delivers average specific capacities of 442.3, 425.0, 391.7, 371.7, 352.6, 325.2, and 270.6 mAh g^{-1}, respectively. When the current density is restored to 0.1 A g^{-1}, the capacity rapidly recovers to above 440.0 mAh g^{-1}, demonstrating excellent rate reversibility. Moreover, the GCD profiles recorded at different current densities retain similar overall shapes (Figure 5f), further confirming the robust and rapid charge-storage behavior of NiVOH. By comparison, $H_2V_3O_8$ exhibits a distinctly lower reversible capacity under identical conditions (Figure S7).

To clarify the effect of Ni content, samples with different Ni incorporation levels were compared (Figures S8 and S9). Increasing Ni content generally raises the initial specific capacity, whereas excessive incorporation accelerates capacity fading. Accordingly, NiVOH-3 exhibits poorer long-term retention than optimized NiVOH despite its relatively high initial capacity. This trend reflects a composition-dependent balance among the Ni/V ratio, hydration state, and the extent of structural reconstruction. At the optimized Ni/V ratio, Ni incorporation renders the NiVOH

16163028, 0, Downloaded from https://advanced.onlinelibrary.wiley.com/doi/10.1002/adfm.78757 by Southeast University, Wiley Online Library on [10/10/2026]. See the Terms and Conditions (https://onlinelibrary.wiley.com/terms-and-conditions) on Wiley Online Library for rules of use; OA articles are governed by the applicable Creative Commons License

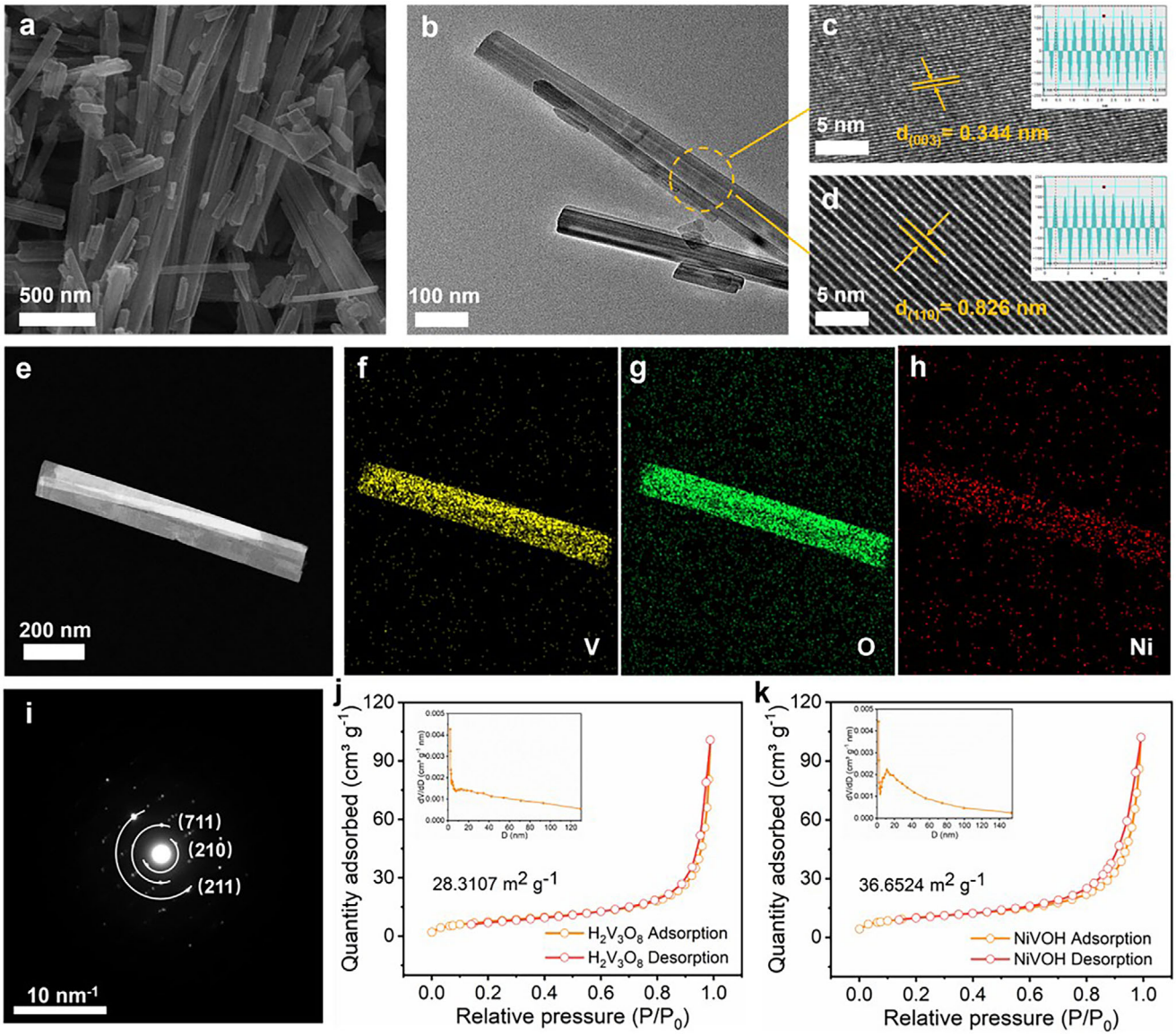

FIGURE 4 | Morphological and microstructural characterization: (a) SEM image. (b) TEM image. (c,d) HRTEM images. (e) STEM image of NiVOH. (f–h) corresponding elemental mappings of V, O, and Ni. (i) SAED pattern of NiVOH. N_2 adsorption–desorption isotherms of (j) $H_2V_3O_8$ and (k) NiVOH, with insets showing the corresponding pore-size distributions.

framework more open while retaining continuous hydrated galleries, and moderate nickel-vanadate-like reconstruction and associated defects contribute to structural stabilization and charge transport. With further Ni incorporation, excessive reconstruction may disrupt this favorable framework balance, reduce the continuity of hydrated ion-transport pathways and increase site occupation, thereby limiting ion transport and compromising structural stability during cycling [26, 33, 50–53]. These results suggest that optimized NiVOH achieves a more favorable balance between ion accessibility and framework stability, thereby supporting its rate capability and cycling durability.

To validate the theoretical screening results, the electrochemical performances of vanadium oxides incorporating different metal ions were further compared. As shown in Figure 5g and Figure S10, NiVOH consistently exhibits the best overall capacity and cycling performance among CuVOH, MgVOH, AlVOH, and ZrVOH over a wide range of current densities. This experimental trend agrees well with the DFT results in Figure 1, which reveal the favorable electronic structure and the lowest Zn^{2+} migration barrier for NiVOH. Finally, as shown in Figure 5h and Table S2, NiVOH delivers competitive overall electrochemical performance compared with previously reported vanadium-based cathodes for aqueous zinc-ion batteries.

2.4 | Kinetic Analysis and Mechanism Discussion

To further elucidate the origin of the superior rate capability of NiVOH, a series of kinetic analyses were performed. The charge-storage kinetics were first investigated by cyclic voltammetry at scan rates ranging from 0.2 to 1.0 mV s^{-1}. As shown in Figure 6a, the overall CV profiles and characteristic redox features are well preserved with increasing scan rate, accompanied by moderate

16163028, 0, Downloaded from https://advanced.onlinelibrary.wiley.com/doi/10.1002/adfm.78757 by Southeast University, Wiley Online Library on [10/10/2026]. See the Terms and Conditions (https://onlinelibrary.wiley.com/terms-and-conditions) on Wiley Online Library for rules of use; OA articles are governed by the applicable Creative Commons License

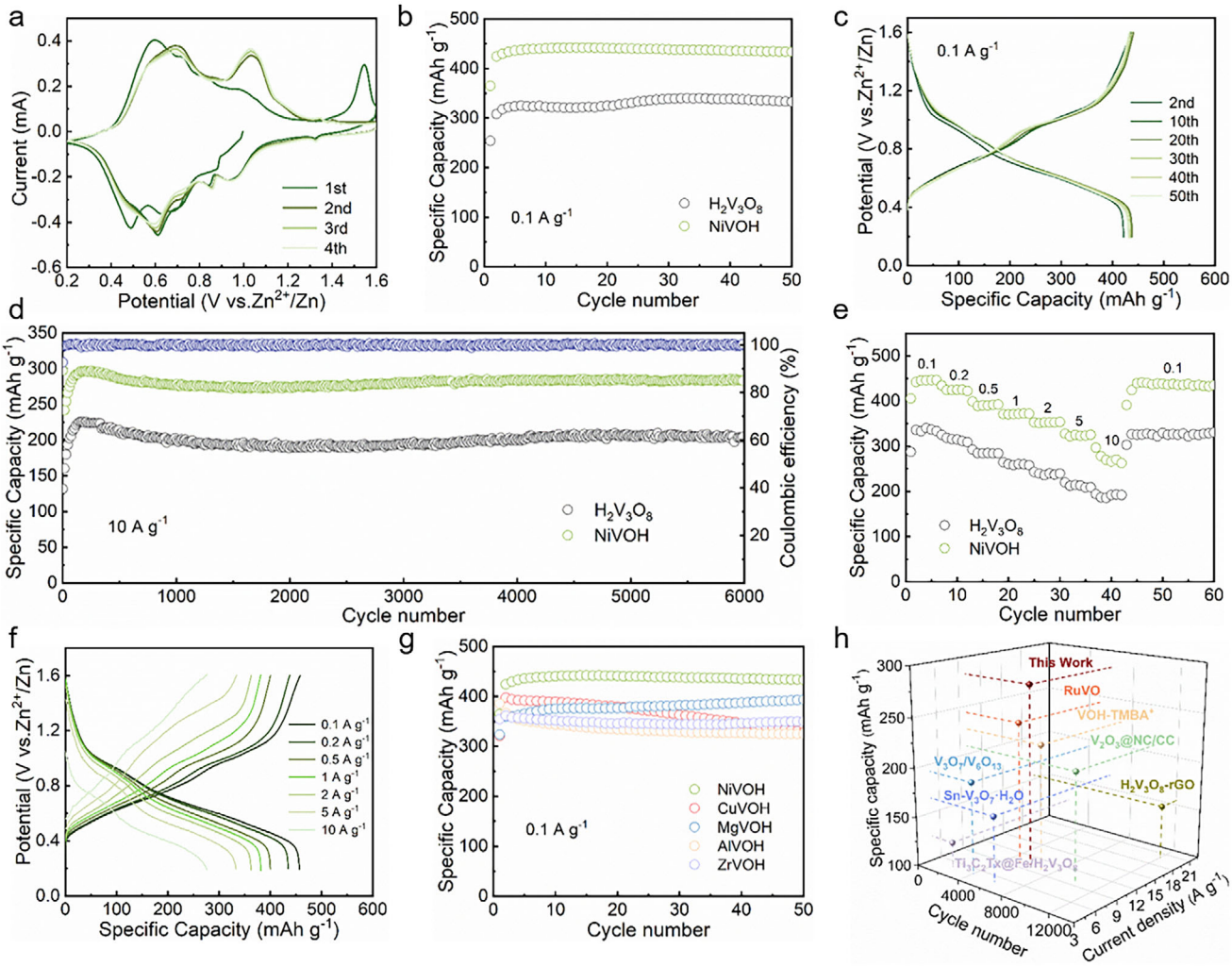

FIGURE 5 | Electrochemical performance: (a) CV curves of NiVOH for the first four cycles within 0.2–1.6 V. (b) Cycling performances of $H_2V_3O_8$ and NiVOH at 0.1 A g^{-1}. (c) GCD profiles of NiVOH at selected cycles at 0.1 A g^{-1}. (d) Cycling performances of $H_2V_3O_8$ and NiVOH at 10 A g^{-1}. (e) Rate performances of $H_2V_3O_8$ and NiVOH. (f) GCD profiles of NiVOH at different current densities. (g) Cycling performances of NiVOH, CuVOH, MgVOH, AlVOH, and ZrVOH at 0.1 A g^{-1}. (h) Comparison of the performance of NiVOH with previously reported vanadium-based cathodes.

polarization-induced peak shifts. The relationship between the peak current and scan rate can be expressed as:

$$i = av^b \tag{1}$$

where i is the peak current, v is the scan rate, and a and b are adjustable parameters. A b value approaching 0.5 generally indicates a diffusion-controlled process, whereas a b value close to 1.0 is characteristic of surface-controlled charge storage. As shown in Figure 6b, the calculated b values for Peaks 1–4 are 0.71, 0.99, 0.90, and 0.84, respectively. These values indicate that NiVOH follows a mixed charge-storage mechanism involving both diffusion-controlled and surface-controlled processes, with Peaks 2–4 exhibiting pronounced surface-controlled capacitive characteristics. The capacitive contribution was further quantified according to:

$$i\ (V) = k_1\ v + k_2 v^{\frac{1}{2}} \tag{2}$$

where $k_1 v$ and $k_2 v^{\frac{1}{2}}$ represent the capacitive-controlled and diffusion-controlled current contributions, respectively [54]. As summarized in Figure 6c, the capacitive contribution of NiVOH progressively increases from 70.1% at 0.2 mV s^{-1} to 75.2%, 77.9%, 81.0%, and 84.4% at 0.4, 0.6, 0.8, and 1.0 mV s^{-1}, respectively. The corresponding capacitive regions at different scan rates are presented in Figure S11. Notably, NiVOH exhibits a capacitive contribution of 84.4% at 1.0 mV s^{-1} (Figure 6d), markedly higher than the 60.7% obtained for $H_2V_3O_8$ (Figure 6e). The enhanced capacitive response reduces the dependence of charge storage on long-range solid-state diffusion and therefore contributes to the superior high-rate performance of NiVOH. This kinetic enhancement can be attributed to the Ni-regulated interlayer environment, increased oxygen-vacancy concentration, more accessible hydrated galleries, and enlarged specific surface area, which collectively improve the accessibility of redox-active sites and shorten ion-transport distances [26, 41, 55].

The self-discharge behavior was subsequently evaluated by charging the electrodes to 1.6 V, followed by open-circuit

16163028, 0, Downloaded from https://advanced.onlinelibrary.wiley.com/doi/10.1002/adfm.78757 by Southeast University, Wiley Online Library on [10/10/2026]. See the Terms and Conditions (https://onlinelibrary.wiley.com/terms-and-conditions) on Wiley Online Library for rules of use; OA articles are governed by the applicable Creative Commons License

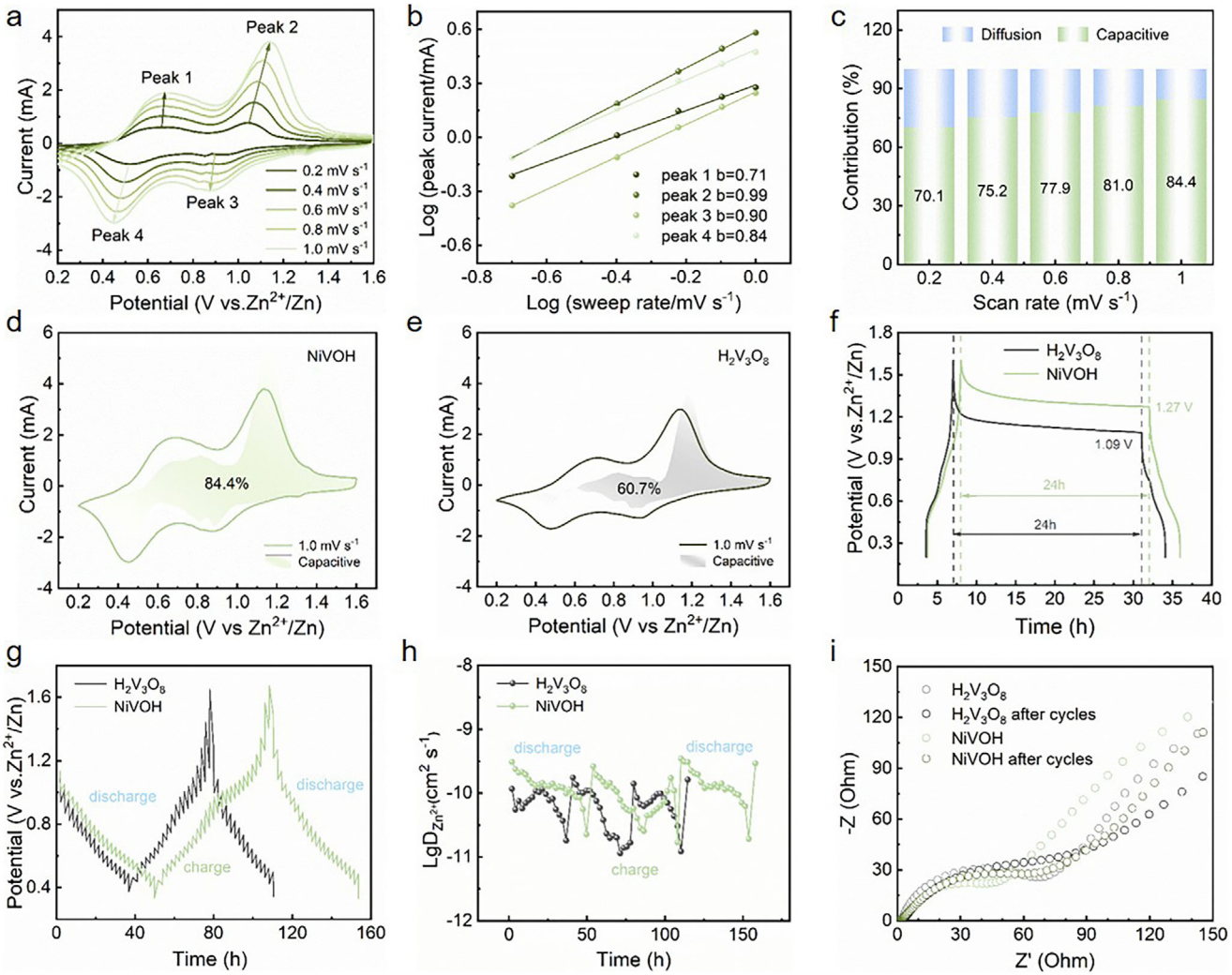

FIGURE 6 | Electrochemical kinetics and ion-transport characteristics: (a) CV curves of NiVOH at scan rates ranging from 0.2 to 1.0 mV s^{-1}. (b) Linear relationships between log *i* and log *v* for the selected redox peaks. (c) Capacitive- and diffusion-controlled contributions of NiVOH at different scan rates. Capacitive contributions of (d) NiVOH and (e) $H_2V_3O_8$ at 1.0 mV s^{-1}. (f) Self-discharge profiles of $H_2V_3O_8$ and NiVOH. (g) GITT profiles and (h) corresponding apparent Zn^{2+} diffusion coefficients of $H_2V_3O_8$ and NiVOH. (i) Nyquist plots of $H_2V_3O_8$ and NiVOH before and after cycling.

relaxation for 24 h (Figure 6f). After relaxation, NiVOH retains an open-circuit voltage of 1.27 V, substantially higher than the 1.09 V maintained by $H_2V_3O_8$. The improved open-circuit-voltage retention of NiVOH may arise from the cooperative effects of oxygen-vacancy-related defect states, Ni—O-mediated framework stabilization, and the hydrated interlayer environment. Defect-assisted charge transfer may alleviate local polarization, whereas Ni—O coupling and electrostatic screening by interlayer water may suppress spontaneous structural relaxation, irreversible Zn–host interactions, and related parasitic reactions during open-circuit relaxation [26, 33, 56, 57]. The ion-transport kinetics were further examined using the galvanostatic intermittent titration technique (GITT). As shown in Figure 6g, both electrodes exhibit characteristic potential responses during successive current-pulse and relaxation steps, reflecting the multistep insertion and extraction reactions of charge carriers in the hydrated vanadium oxide framework [58, 59]. The apparent Zn^{2+} diffusion coefficients derived from the GITT profiles are presented in Figure 6h. Throughout most of the charge and discharge processes, the apparent Zn^{2+} diffusion coefficient of NiVOH is approximately half an order of magnitude higher than that of $H_2V_3O_8$, demonstrating faster apparent ion diffusion. This result is consistent with the lower Zn^{2+} migration barrier predicted for NiVOH by the DFT calculations and can be rationalized by the Ni-induced regulation of the interlayer environment and host structure. Specifically, the more open hydrated galleries provide sufficient space for ion migration, while interlayer water partially screens the strong electrostatic interaction between the inserted ions and the V—O framework. In addition, the Ni-induced lattice defects and partial structural reconstruction may create more accessible ion-transport pathways, thereby further accelerating ion migration within the electrode [16, 17, 29, 30].

Electrochemical impedance spectroscopy (EIS) was employed to probe the interfacial charge-transfer behavior of the two electrodes before and after cycling (Figure 6i). All Nyquist plots consist of a depressed arc in the high-to-medium-frequency region and an inclined line in the low-frequency region, which are associated with interfacial charge-transfer

16163028, 0, Downloaded from https://advanced.onlinelibrary.wiley.com/doi/10.1002/adfm.78757 by Southeast University, Wiley Online Library on [10/10/2026]. See the Terms and Conditions (https://onlinelibrary.wiley.com/terms-and-conditions) on Wiley Online Library for rules of use; OA articles are governed by the applicable Creative Commons License

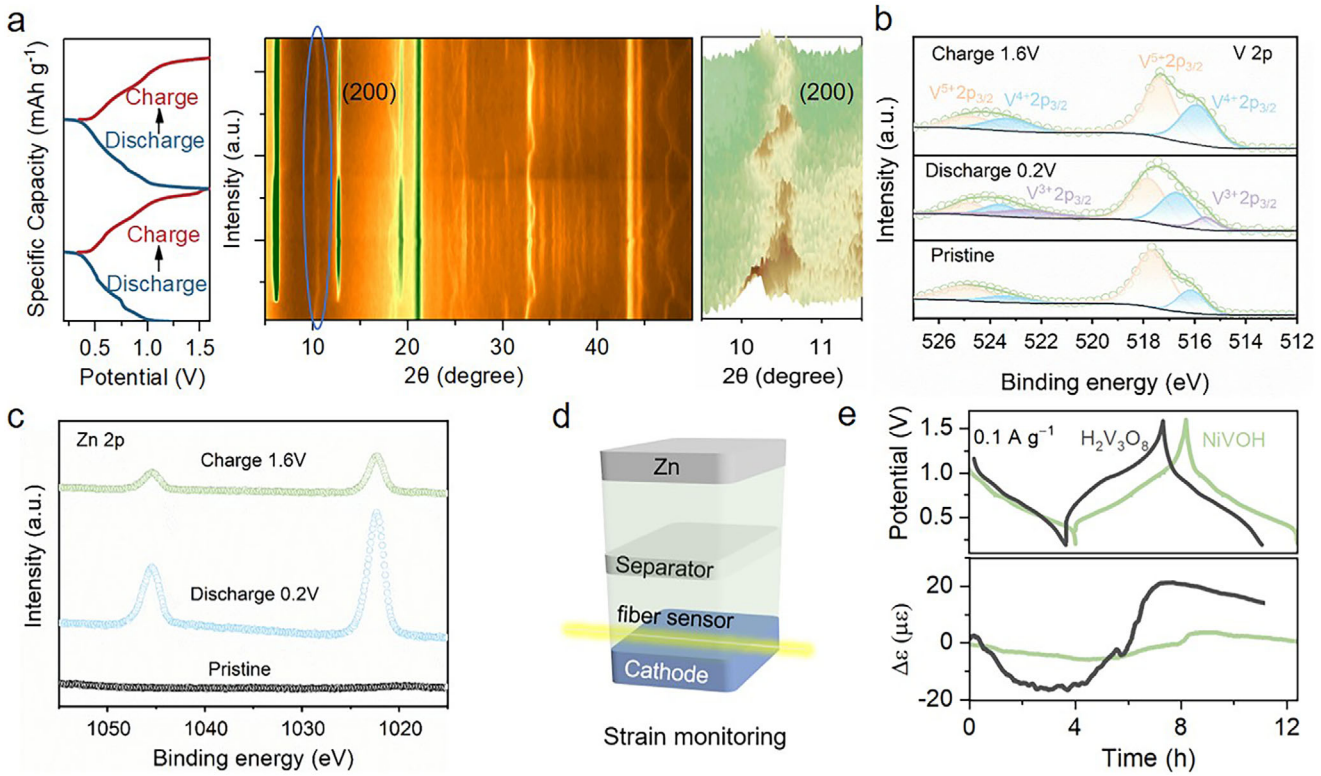

FIGURE 7 | Zn-storage mechanism and chemo-mechanical response: (a) In situ XRD patterns of NiVOH during the first two charge–discharge cycles. Ex situ high-resolution XPS spectra of (b) V 2p and (c) Zn 2p for NiVOH. (d) Schematic illustration of the fiber-optic sensor configuration for real-time electrode strain monitoring. (e) Corresponding galvanostatic charge–discharge profiles and electrode-level strain responses of $H_2V_3O_8$ and NiVOH at 0.1 A g^{-1}.

and ion-diffusion processes, respectively [25–28]. NiVOH exhibits a smaller high-frequency arc than $H_2V_3O_8$ before cycling, indicating more favorable interfacial charge-transfer kinetics. After cycling, NiVOH still maintains a comparatively lower interfacial impedance, suggesting that its favorable charge-transfer characteristics are better preserved during repeated ion insertion and extraction. The reduced impedance can be attributed to the Ni-induced electronic-structure regulation and increased oxygen-vacancy concentration, together with the improved electrolyte accessibility arising from the more open interlayer structure and mesoporous architecture [33–36].

2.5 | Zn-Storage Mechanism and Electrochemical-Mechanical Analysis

To directly elucidate the structural evolution of NiVOH during electrochemical cycling, in situ XRD was performed over the first two charge–discharge cycles. Owing to the relatively low crystallinity resulting from the rapid one-step hydrothermal synthesis, only the $H_2V_3O_8$-related (200) reflection can be reliably tracked, while information for all other crystal planes is unavailable (Figure 7a). During discharge, the (200) reflection gradually shifts toward a higher 2θ angle, indicating a decrease in the corresponding d_{200} spacing and a contraction of the lattice along this crystallographic direction. Upon subsequent charging, the peak reversibly returns toward its initial position. This reversible peak evolution is reproduced during the second cycle, demonstrating highly reversible structural breathing of the NiVOH framework. In addition to the reversible shift of the $H_2V_3O_8$-related (200) reflection, transient diffraction features are observed at approximately 6.5° and 12.9°. These peaks can be assigned to the basal reflections of $Zn_x(CF_3\ SO_3\ )_y\ (OH)_{2x-y}\ \cdot nH_2\ O$ (basic zinc salt), which is reversibly precipitated and dissolved during discharge and charge, respectively. The reflection near 32.5° contains overlapping contributions from the basic zinc salt and the NiVOH host framework and is therefore not assigned to a single phase [26, 33].

The reversible charge-storage chemistry was further investigated using ex situ XPS. As shown in Figure 7b, the contribution from lower-valence vanadium increases markedly after discharge to 0.2 V, indicating the reduction of vanadium during ion insertion. When the electrode is subsequently charged to 1.6 V, the V^{3+} component largely disappears and the V^{5+} contribution is substantially restored, confirming the high reversibility of the multistep vanadium redox reactions. The Zn 2p spectra provide direct evidence for Zn^{2+} participation in the electrochemical reaction (Figure 7c). No detectable Zn signal is observed in the pristine electrode, whereas two pronounced Zn 2p peaks appear after discharge to 0.2 V, confirming the insertion of Zn^{2+} into the NiVOH electrode. After charging to 1.6 V, the Zn-related signals decrease substantially, demonstrating the reversible extraction of Zn^{2+} [56, 58, 59]. The weak residual Zn signal in the charged state may arise from a small fraction of strongly bound or incompletely extracted Zn species at defect sites or within the reconstructed framework.

16163028, 0, Downloaded from https://advanced.onlinelibrary.wiley.com/doi/10.1002/adfm.78757 by Southeast University, Wiley Online Library on [10/10/2026]. See the Terms and Conditions (https://onlinelibrary.wiley.com/terms-and-conditions) on Wiley Online Library for rules of use; OA articles are governed by the applicable Creative Commons License

To further quantify the mechanical response associated with the ion-storage process, a fiber Bragg grating (FBG) sensor was embedded between the cathode and separator to monitor the electrode-level strain in real time (Figure 7d). The sensing principle is illustrated in Figure S12. In short, deformation of the FBG changes its grating period and effective refractive index, producing a measurable shift in the Bragg wavelength that can be converted into strain [28, 60]. FBG reflects the integrated electrode-level response and therefore cannot be directly equated with the lattice strain of single crystals; nevertheless, under otherwise comparable conditions, its evolution can indirectly reflect underlying lattice changes. As shown in Figure 7e, both NiVOH and $H_2V_3O_8$ exhibit decreasing strain during discharge and increasing strain during charge, qualitatively following the charge/discharge-dependent structural response observed by in situ XRD. Notably, NiVOH displays substantially smaller strain fluctuations than $H_2V_3O_8$ throughout both discharge and charge, further demonstrating that Ni incorporation effectively mitigates the structural deformation induced by repeated ion insertion and extraction. This enhanced mechanical stability can be attributed to the complementary roles of the coexisting structural domains: the residual $H_2V_3O_8$ domains preserve open ion-transport pathways, whereas the Ni-containing reconstructed domains and the interlayer anchoring effect of Ni pillars strengthen the structural coupling between adjacent V–O layers. In addition, the increased structural-water content may provide a more compliant buffering environment to accommodate dimensional changes of the electrode during cycling [13–17, 34].

3 | Conclusion

In summary, a dual-chamber-assisted high-temperature mixing hydrothermal process was developed to prepare NiVOH through the coupled glucose-driven reconstruction of V_2O_5 and synchronous Ni^{2+} incorporation. Theoretical screening and comparative experiments consistently identify Ni^{2+} as the most effective among Cu^{2+}, Mg^{2+}, Ni^{2+}, Al^{3+}, and Zr^{4+} for regulating the host electronic structure and facilitating Zn^{2+} migration. Optimized Ni incorporation not only expands the parent lattice, but also produces a hydrated and defect-rich framework comprising retained $H_2V_3O_8$ domains and Ni-containing reconstructed domains. The former preserve accessible ion-transport galleries, whereas the latter provide structural constraint against cycling-induced deformation. Accordingly, NiVOH delivers 433.4 mAh g^{-1} after 50 cycles at 0.1 A g^{-1} and sustains 282.6 mAh g^{-1} after 6000 cycles at 10 A g^{-1}. In situ XRD and ex situ XPS verify reversible Zn^{2+} insertion/extraction, while fiber-optic strain measurements demonstrate markedly suppressed electrode-level deformation. This work provides new insights into the preparation of high-performance cathodes for AZIBs.

Author Contributions

Zhihan Kong: conceptualization, methodology, data curation, investigation, validation, formal analysis, visualization, writing – original draft, software, writing – review and editing. **Penghua Liang**: conceptualization, methodology, writing – review and editing, data curation, validation, software. **Tengyu Yao**: software, validation, visualization, formal analysis, data curation. **Xinyue Mu**: investigation, formal analysis, data curation. **Dingwei Ji**: data curation, validation. **Longbiao Yu**: validation, data curation. **Feier Wang**: validation, data curation. **Jing Wang**: funding acquisition, supervision, resources. **Kang Yan**: funding acquisition, project administration, supervision, resources. **Jun Guo**: conceptualization, methodology, writing – review and editing, visualization, data curation, supervision, project administration. **Laifa Shen**: software, supervision, writing – review and editing, project administration, resources, conceptualization. **Linfeng Hu**: supervision, resources, software, project administration, writing – review and editing, conceptualization. **Kongjun Zhu**: funding acquisition, conceptualization, methodology, data curation, supervision, validation, project administration, resources, writing – review and editing.

Acknowledgements

This work was financially supported by the National Natural Science Foundation of China (Grant Number. 52372200), the Frontier Technologies R&D Program of Jiangsu (Grant Number. BF2024033), China Postdoctoral Science Foundation (2025M784326), the Postdoctoral Fellowship Program of CPSF (GZC20262008), and State Key Laboratory of Mechanics and Control for Mechanical Structures (Nanjing University of Aeronautics and Astronautics) (Grant Number. MCAS-S-0326G05).

Conflicts of Interest

The authors declare no conflicts of interest.

Data Availability Statement

The data that support the findings of this study are available from the corresponding author upon reasonable request.

References

1. M. Li, J. Lu, Z. W. Chen, and K. Amine, "30 Years of Lithium-Ion Batteries," *Advanced Materials* 30 (2018): 24.

2. Z. W. Huang, S. C. Han, J. J. Pang, et al., "From Modification to Regeneration: Synergistic Advances in Olivine $LiMn_xFe_{1-x}PO_4$ Cathodes and Closed-Loop Recycling of Spent $LiFePO_4$," *Advanced Functional Materials* 36 (2026): 26.

3. S. Kalnaus, N. J. Dudney, A. S. Westover, E. Herbert, and S. Hackney, "Solid-State Batteries: The Critical Role of Mechanics," *Science* 381 (2023): 1300, https://doi.org/10.1126/science.abg5998.

4. Y. J. Li, S. Kumar, G. L. Yang, et al., "The Contrast Between Monovalent and Multivalent Metal Battery Anodes," *Science* 389 (2025): 12, https://doi.org/10.1126/science.adl5482.

5. Y. Dong, H. L. Hu, P. Liang, et al., "Dissolution, Solvation and Diffusion in Low-Temperature Zinc Electrolyte Design," *Nature Reviews Chemistry* 9 (2025): 102–117, https://doi.org/10.1038/s41570-024-00670-7.

6. M. Song, H. Tan, D. L. Chao, and H. J. Fan, "Recent Advances in Zn-Ion Batteries," *Advanced Functional Materials* 28 (2018): 27, https://doi.org/10.1002/adfm.201802564.

7. G. J. Li, L. Sun, S. L. Zhang, et al., "Developing Cathode Materials for Aqueous Zinc Ion Batteries: Challenges and Practical Prospects," *Advanced Functional Materials* 34 (2024): 26.

8. M. C. Tang, Q. Liu, X. H. Zou, B. Zhang, and L. An, "High-Energy-Density Aqueous Zinc-Ion Batteries: Recent Progress, Design Strategies, Challenges, and Perspectives," *Advanced Materials* 37 (2025): 40.

9. R. Sinha, X. S. Xie, Y. Yang, et al., "Failure Mechanisms and Strategies for Vanadium Oxide-Based Cathode in Aqueous Zinc Batteries," *Advanced Energy Materials* 15 (2025): 41, https://doi.org/10.1002/aenm.202404815.

10. M. Y. Yan, P. He, Y. Chen, et al., "Water-Lubricated Intercalation in $V_2O_5{\cdot}nH_2O$ for High-Capacity and High-Rate Aqueous Rechargeable Zinc Batteries," *Advanced Materials* 30 (2018): 6.

16163028, 0, Downloaded from https://advanced.onlinelibrary.wiley.com/doi/10.1002/adfm.78757 by Southeast University, Wiley Online Library on [10/10/2026]. See the Terms and Conditions (https://onlinelibrary.wiley.com/terms-and-conditions) on Wiley Online Library for rules of use; OA articles are governed by the applicable Creative Commons License

11. C. F. Liu, Z. Neale, J. Q. Zheng, et al., "Expanded Hydrated Vanadate for High-performance Aqueous Zinc-ion Batteries," *Energy & Environmental Science* 12 (2019): 2273–2285, https://doi.org/10.1039/C9EE00956F.

12. C. F. Liu, M. Tian, M. S. Wang, et al., "Catalyzing Zinc-ion Intercalation in Hydrated Vanadates for Aqueous Zinc-ion Batteries," *Journal of Materials Chemistry A* 8 (2020): 7713–7723, https://doi.org/10.1039/D0TA01468K.

13. X. Ding, Q. Y. Zhu, Y. Fan, et al., "High-entropy V-Based Cathode for High-Capacity and Long-Life Aqueous Zinc-ion Battery," *Nano Energy* 136 (2025): 110701, https://doi.org/10.1016/j.nanoen.2025.110701.

14. X. Ding, J. R. Le, Y. B. Yang, et al., "A High-Entropy Zero-Strain V-Based Cathode for High Performance Aqueous Zinc-ion Batteries," *Energy Storage Materials* 76 (2025): 104098.

15. D. M. Dai, Y. Chen, B. Li, et al., "Drastically Promoting Rate Capability via Dual-Cations Intercalation of V_2O_5 Enabling Rapid Zinc-Ion Storage," *Small* 21 (2025): 9, https://doi.org/10.1002/smll.202408596.

16. R. Li, F. Xing, T. Y. Li, et al., "Intercalated Polyaniline in V_2O_5 as a Unique Vanadium Oxide Bronze Cathode for Highly Stable Aqueous Zinc Ion Battery," *Energy Storage Materials* 38 (2021): 590–598, https://doi.org/10.1016/j.ensm.2021.04.004.

17. S. Zhao, S. Wang, J. B. Guo, et al., "Sodium-Ion and Polyaniline Co-Intercalation Into Ammonium Vanadate Nanoarrays Induced Enlarged Interlayer Spacing as High-Capacity and Stable Cathodes for Flexible Aqueous Zinc-Ion Batteries," *Advanced Functional Materials* 33 (2023): 11.

18. J. Y. Sun, L. Zhang, F. B. Li, et al., "Crystalline-Amorphous Phase and Oxygen Vacancies Synergistically Regulate Vanadium Electronic States for Unleashing Zinc-Ion Storage Performance," *Advanced Functional Materials* 35 (2025): 14.

19. W. Liu, X. Y. Liu, F. H. Ning, et al., "Fabrication of a Heterovalent Dual-Cation Pre-Embedded Hydrated Vanadium Oxide Cathode for High-Performance Zinc Ion Storage," *Journal of Materials Chemistry A* 12 (2024): 11883–11894, https://doi.org/10.1039/D4TA00376D.

20. C. Zhang, Y. Huang, X. E. Xu, et al., "Bulk-to-Surface Co-Modification of Layered Hydrated Vanadate Cathode for Aqueous Zinc Ion Batteries," *Energy & Environmental Science* 17 (2024): 4090–4103, https://doi.org/10.1039/D4EE00535J.

21. D. Chen, H. L. Chen, C. F. Du, et al., "From Vanadium Slag to Multi-Cation-Intercalated $V_2O_5{\cdot}nH_2O$: Low-Cost Direct Synthesis and High-Performance Aqueous Battery Application," *Journal of Materials Chemistry A* 10 (2022): 5479–5487, https://doi.org/10.1039/D1TA10545K.

22. Y. J. Wang, Y. M. Fan, X. D. Chen, et al., "Synergistic Effects of Structural and Electronic Dual Engineering for Ultra-Stable Aqueous Zinc-Ion Batteries," *InfoMat* 7 (2025): 13.

23. X. Y. Hu, S. Y. Gao, T. E. Lin, et al., "Iodine-Doped Sodium Vanadate Cathode for Improved Zn Ion Diffusion Kinetics," *Advanced Materials* 37 (2025): 11.

24. H. B. Song, Y. F. Cui, Y. F. Li, et al., "Alcohol Molecule Coupling: A Universal Approach to Modulating Amorphousness in Vanadium-Based Cathodes for High-Rate and Durable Aqueous Zinc-ion Batteries," *Science Advance* 11 (2025): 14.

25. Y. Y. Gu, Y. Zhang, M. D. Wei, et al., "Selective Adsorption of MAPTAC Constructs Water-Deficient Electric Double Layer for Enhanced Zinc Battery Performance," *Small* 21 (2025): 13.

26. Z. Chen, H. B. Liu, S. Y. Fan, et al., "Inhibition of Vanadium Cathode Dissolution in Zinc-Ion Batteries on Thermodynamics and Kinetics by Guest Pre-Intercalation," *Advanced Energy Materials* 14 (2024): 9.

27. P. H. Liang, T. F. Xu, K. J. Zhu, et al., "Heterogeneous Interface-Boosted Zinc Storage of $H_2V_3O_8$ Nanowire/$Ti_3C_2T_x$ MXene Composite Toward High-Rate and Long Cycle Lifespan Aqueous Zinc-ion Batteries," *Energy Storage Materials* 50 (2022): 63–74, https://doi.org/10.1016/j.ensm.2022.05.010.

28. D. W. Ji, J. Guo, Z. H. Kong, et al., "Achieving Near-Zero-Strain via Volumetric Neutralization in an $H_2V_3O_8$ /MXene/VO_2 Cathode for Durable Zinc-Ion Batteries," *Advanced Functional Materials* 36 (2026): 11, https://doi.org/10.1002/adfm.74811.

29. S. Zhang, Z. X. Gao, D. D. Zhang, and J. Cao, "V_2O_5/$V_3O_7H_2O$ Heterostructures for Aqueous Zinc-ion Energy Storage," *Chemical Engineering Journal* 535 (2026): 13.

30. A. B. Olabintan, T. A. Saleh, and A. Al-Ahmed, "Co Doped $V_3O_7{\cdot}H_2O$ Nanobelt Cathode With a Three-stage Ion Intercalation Mechanism for Enhancing the Electrochemical Kinetics of Aqueous Zinc-ion Batteries," *Journal of Energy Storage* 156 (2026): 11.

31. S. K. Maddhi, H. Bandi, and J. S. Yu, "Enhanced Zn^{2+} Storage Performance of V_3O_7@CsV_3O_8 Nanocomposite Cathode for Aqueous Zinc-ion Batteries," *Journal of Energy Storage* 173 (2026): 122659, https://doi.org/10.1016/j.est.2026.122659.

32. Y. Liu, X. Wang, Z. S. Wu, Y. R. Cho, and X. Wu, "Conductive Metal–Organic Frameworks Anchoring on $V_3O_7{\cdot}H_2O$ Nanobelts Toward High-Capacity and Long-Life Zinc-Ion Batteries," *Advanced Functional Materials* 35 (2025): 9.

33. D. D. Zhang, J. Cao, C. W. Yang, et al., "Highly Stable Aqueous Zn-Ion Batteries Achieved by Suppressing the Active Component Loss in Vanadium-Based Cathode," *Advanced Energy Materials* 15 (2025): 11.

34. Y. W. Shi, B. S. Yin, Y. Sun, et al., "Mg Ions Intercalated With $V_3O_7{\cdot}H_2O$ to Construct Ultrastable Cathode Materials for Aqueous Zinc-ion Batteries," *Chemical Communications* 60 (2024): 8597–8600, https://doi.org/10.1039/D4CC03201B.

35. Q. Q. He, J. Bai, M. D. Xue, et al., "Polypyride Intercalation Boosting the Kinetics and Stability of $V_3O_7{\cdot}H_2O$ Cathodes for Aqueous Zinc-ion Batteries," *Journal of Energy Chemistry* 97 (2024): 361–370, https://doi.org/10.1016/j.jechem.2024.05.051.

36. Q. Zang, X. J. Cheng, S. J. Chen, et al., "Oxygen Defect Engineering Triggered by S-Doping Boosts the Performance of $H_2V_3O_8$ Nanobelts for Aqueous Zn-ion Storage," *Chemical Engineering Journal* 452 (2023): 139396, https://doi.org/10.1016/j.cej.2022.139396.

37. H. Y. Wen, Y. W. Shi, B. S. Yin, et al., "Conductive Polymer Networks: Enabling High-performance Zinc-ion Batteries via Dual-ion Storage Mechanism and Structural Suppression," *Applied Surface Science* 713 (2025): 164351, https://doi.org/10.1016/j.apsusc.2025.164351.

38. W. H. Mi, B. S. Yin, H. X. Gu, et al., "PVP Pre-Intercalation Engineering Combined With the V^{4+}/V^{5+} Dual-valence Modulation Strategy for Energy Storage in Aqueous Zinc-ion Batteries," *Nanoscale Horizons* 10 (2025): 1365–1376, https://doi.org/10.1039/D5NH00236B.

39. Y. X. Wang, S. Q. Wei, Z. H. Qi, et al., "Intercalant-induced Vt_2G Orbital Occupation in Vanadium Oxide Cathode Toward Fast-Charging Aqueous Zinc-ion Batteries," *Proceedings of the National Academy of Sciences of the United States of America* 120 (2023): 8.

40. H. Liu, L. Yang, T. Shen, et al., "Distorting Local Structures to Modulate Ligand Fields in Vanadium Oxide for High-Performance Aqueous Zinc-Ion Batteries," *ACS Nano* 19 (2025): 9132–9143, https://doi.org/10.1021/acsnano.4c18250.

41. J. D. Guo, J. X. Liu, W. B. Ma, et al., "Vanadium Oxide Intercalated With Conductive Metal–Organic Frameworks With Dual Energy-Storage Mechanism for High Capacity and High-Rate Capability Zn Ion Storage," *Advanced Functional Materials* 33 (2023): 9, https://doi.org/10.1002/adfm.202302659.

42. J. H. Zhang, W. B. Li, J. J. Wang, et al., "Engineering p-Band Center of Oxygen Boosting H^+ Intercalation in δ-MnO_2 for Aqueous Zinc Ion Batteries," *Angewandte Chemie International Edition* 62 (2023): 10.

43. Y. H. Xu, G. N. Zhang, X. X. Wang, et al., "Efficient Modulation d/p-Band Center Proximity in Birnessite-Type MnO_2 by Cation/Anion Co-Doping for Enhanced Dual-Ion Storage," *Advanced Functional Materials* 35 (2025): 14.

16163028, 0, Downloaded from https://advanced.onlinelibrary.wiley.com/doi/10.1002/adfm.78757 by Southeast University, Wiley Online Library on [10/10/2026]. See the Terms and Conditions (https://onlinelibrary.wiley.com/terms-and-conditions) on Wiley Online Library for rules of use; OA articles are governed by the applicable Creative Commons License

44. Y. Liu, Y. Yuan, R. Wang, et al., "Computational Studies for Aqueous Zinc-Ion Secondary Batteries," *Sustainable Engineering Novit* 1 (2025): 6.

45. F. Zhang, M. Du, Z. Y. Miao, et al., "Oxygen Vacancies and N-Doping in Organic–Inorganic Pre-Intercalated Vanadium Oxide for High-Performance Aqueous Zinc-ion Batteries," *InfoMat* 4 (2022): 13, https://doi.org/10.1002/inf2.12346.

46. F. G. Liang, M. Chen, S. C. Zhang, et al., "Electrochemical Activation in Vanadium Oxide With Rich Oxygen Vacancies for High-Performance Aqueous Zinc-Ion Batteries," *ACS Sustainable Chemistry & Engineering* 12 (2024): 5117–5128, https://doi.org/10.1021/acssuschemeng.3c07655.

47. Q. Zong, W. Du, C. F. Liu, et al., "Enhanced Reversible Zinc Ion Intercalation in Deficient Ammonium Vanadate for High-Performance Aqueous Zinc-Ion Battery," *Nano-Micro Letters* 13 (2021): 15, https://doi.org/10.1007/s40820-021-00641-3.

48. K. W. Nam, S. S. Park, R. dos Reis, et al., "Conductive 2D Metal-Organic Framework for High-Performance Cathodes in Aqueous Rechargeable Zinc Batteries," *Nature Communications* 10 (2019): 10, https://doi.org/10.1038/s41467-019-12857-4.

49. Y. H. Dai, C. Y. Zhang, J. W. Li, et al., "Inhibition of Vanadium Cathodes Dissolution in Aqueous Zn-Ion Batteries," *Advanced Materials* 36 (2024): 9.

50. R. K. Li, R. X. Zhao, A. C. Tang, et al., "Hydration-Driven Structural Heterogeneity for Robust Zn^{2+} Storage in Vanadium Oxide Cathodes," *Advanced Functional Materials* 36 (2026): 11.

51. P. Byeon, Y. Hong, H. Bin Bae, J. Shin, J. W. Choi, and S. Y. Chung, "Atomic-Scale Unveiling of Multiphase Evolution During Hydrated Zn-ion Insertion in Vanadium Oxide," *Nature Communications* 12 (2021): 11, https://doi.org/10.1038/s41467-021-24700-w.

52. H. H. Niu, H. Liu, L. Yang, et al., "Impacts of Distorted Local Chemical Coordination on Electrochemical Performance in Hydrated Vanadium Pentoxide," *Nature Communications* 15 (2024): 9, https://doi.org/10.1038/s41467-024-53785-2.

53. Z. C. Jiang, S. T. Zhang, S. X. Wang, et al., "Design of Iron-Based Prussian Blue Analogues via Transition Metal Incorporation for Aqueous Ni–Zn Batteries," *Rare Metals* 44 (2025): 10998–11005, https://doi.org/10.1007/s12598-025-03623-1.

54. V. Augustyn, J. Come, M. A. Lowe, et al., "High-Rate Electrochemical Energy Storage Through Li^+ Intercalation Pseudocapacitance," *Nature Materials* 12 (2013): 518–522, https://doi.org/10.1038/nmat3601.

55. A. Wang, D. H. Liu, L. Yang, et al., "Building stabilized $Cu_{0.17}Mn_{0.03}V_2O_{5-}\square \cdot 2.16H_2O$ Cathode Enables an Outstanding Room-/Low-Temperature Aqueous Zn-ion Batteries," *Carbon Energy* 6 (2024): 11, https://doi.org/10.1002/cey2.512.

56. J. Sun, J. Zhang, S. Y. Wang, et al., "Decoding the Mechanism of Self-Discharge and Optimal Electrolyte Reconfiguration for Advanced Vanadium-Based Aqueous Zinc Batteries," *Energy & Environmental Science* 17 (2024): 4304–4318, https://doi.org/10.1039/D4EE01208A.

57. Y. F. Zhang, S. J. Gao, Q. Li, et al., "Bifunctional Organic Molecule Co-Intercalated Aluminum Vanadate for Highly Reversible Aqueous Zinc-Ion Batteries," *Advanced Functional Materials* 36 (2026): 9.

58. M. Y. Jia, W. H. Zhang, X. P. Cai, et al., "Re-Understanding the Galvanostatic Intermittent Titration Technique: Pitfalls in Evaluation of Diffusion Coefficients and Rational Suggestions," *Journal of Power Sources* 543 (2022): 231843, https://doi.org/10.1016/j.jpowsour.2022.231843.

59. J. W. Wang, H. R. Huang, L. N. Qiao, et al., "An Unconventional Charge Compensation Mechanism for Proton Insertion in Aqueous Zn-ion Batteries," *Journal of Materials Chemistry A* 12 (2024): 31942–31948, https://doi.org/10.1039/D4TA05214E.

60. L. A. Blanquer, F. Marchini, J. R. Seitz, et al., "Optical Sensors for Operando Stress Monitoring in Lithium-Based Batteries Containing Solid-State or Liquid Electrolytes," *Nature Communications* 13 (2022): 14.

Supporting Information

Additional supporting information can be found online in the Supporting Information section.

Supporting File: adfm78757-sup-0001-SuppMat.docx.

16163028, 0, Downloaded from https://advanced.onlinelibrary.wiley.com/doi/10.1002/adfm.78757 by Southeast University, Wiley Online Library on [10/10/2026]. See the Terms and Conditions (https://onlinelibrary.wiley.com/terms-and-conditions) on Wiley Online Library for rules of use; OA articles are governed by the applicable Creative Commons License